Geophys. J. Int. (2005) **163,** 647–662 doi: 10.1111/j.1365-246X.2005.02770.x

Physical model for the downhole orbital vibrator (DOV) – I. Acoustic and borehole seismic radiation

P. C. Leary and L. A. Walter

Geospace Engineering Resources International, 7007 *Pinemont Dr, Houston,* TX 77040-4444, *USA. E-mail: pcleary1@blueyonder.co.uk*

Accepted 2005 August 2. Received 2005 June 1; in original form 2003 May 7

SUMMARY

The downhole orbital vibrator (DOV) applies the Vibroseis principle to borehole seismic sourcing. Accelerations by an internal rotating eccentric mass excite cylindrical pressure waves converted at the wellbore to seismic waves essentially within 20°–30° of the plane normal to the borehole. DOV pressure waves in open water are quantitatively described by a rotating point force radiating acoustic waves with displacement amplitude $u(r) \approx 1/2\, u_0 \gamma R_1/r$, where $R_1 = \pi^2 \rho_{\rm dov}/\rho_{\rm water}\, a^2 \ell/\lambda^2 \approx 1$ mm is the DOV effective size for DOV radius $a \approx 5$ cm, length $\ell \approx 1$ m and acoustic radiation wavelength $\lambda \approx 10$ m, and $u_0 \approx 1\ \mu$m and γ_x are, respectively, the frequency-independent DOV displacement amplitude and the direction cosine of the observer relative to the instantaneous point-force axis in the plane of the rotating point force. Crosswell seismic radiation amplitude, spectrum and angular dependence are quantitatively described by acoustic wave diffraction at a slit with DOV axial cross-section $2a\ell$, followed by conversion to seismic waves at the wellbore. Seismic wave displacement amplitudes $u(r) \approx u_0 \gamma R_2/r$ scale with effective radius $R_2 \approx 2a\ell/\lambda \approx 1$ cm. The frequency dependence of R_2 is observed as linear frequency enhancement of the seismic wavelet spectrum relative to the source wavelet spectrum. DOV borehole *P*- and *S*-wave production peaks strongly in the plane of DOV rotation, with converted *S* waves both parallel to and transverse to the borehole axis. The small effective source sizes $R_1 \approx 1$ mm and $R_2 \approx 1$ cm at operational frequencies 50–350 Hz imply that DOV motion in a borehole is dynamically decoupled from the borehole wall. Dynamic decoupling allows DOV borehole seismic correlation wavelets to be quantitatively modelled in terms of a stable kinematic relation between source and sensor motion. Acoustic and seismic data rule out dipole-source action associated with claims for shear traction and primary *S*-wave radiation from boreholes. The stable linear kinetics of DOV acoustic action in borehole fluids produces (i) useful crosswell seismic signals at offsets to 650–800 m, (ii) negligible tube waves and (iii) stable seismic wavelets suited to *in situ* time-lapse seismic imaging of fluid migration fronts in crustal reservoirs.

Key words: borehole geophysics, flow imaging, radiation patterns, synthetic waveforms, Vibroseis.

1 INTRODUCTION

It is widely understood that reservoir heterogeneity greatly exceeds the ability of reservoir models to predict where geofluids move during oil and gas production, or how groundwater moves in aquifers and in candidate waste repositories. In the hydrocarbon industry, rapidly increasing use of time-lapse seismic imaging reservoir fluid movement is enabling more rational production decisions to improve recovery efficiency and to lower operating costs (Francis & Pennington 2001; Oil & Gas Industry Task Force 2001; de Waal & Calvert 2003; McInally *et al.* 2003; Parker *et al.* 2003). Using time-lapse imaging of injected fluids to map groundwater aquifers is a likely future development (Davis *et al.* 2003; Li 2003). Borehole-based seismic imaging can make use of the inherently quiet, stable and reservoir-proximate downhole environment to achieve higher spatial and temporal *in situ* resolution at lower costs.

Central to advancing the practice of borehole time-lapse reservoir seismic imagery is adapting the principle of land Vibroseis seismic sources to the borehole. Vibroseis sourcing (Waters 1981) distributes source energy over an extended period of time. Impact sources (dynamite, airgun, weight drop) seek to concentrate as much energy as possible in the smallest time and space intervals. The latter form of energy concentrations require large equipment investments, and are typically highly non-linear, substantially non-reproducible and often destructive to the wellbore when conducted downhole. As high-impact equipment cannot easily function in the confines

of a borehole, source energy is usually generated either on or near the land or water surface. However, because of near-surface attenuation of seismic waves, surface sourcing typically constrains seismic frequencies to essentially below 50 Hz, often as low as 30 Hz. Low seismic frequencies greatly complicate imaging of spatially complex, and increasingly small and deep, reservoirs. Non-impact or distributed-energy downhole seismic sourcing allows an order of magnitude increase in spatial/temporal resolution (10–50 → 100–500 Hz) and two-to-three orders of magnitude in reduced power (30–300 KW → 300 W).

Implementing the Vibroseis principle in borehole fluids is straightforward through the centrifugal acceleration produced by an eccentric mass rotating over a range of frequencies. The downhole orbital vibrator (DOV) motor spinning an eccentric weight about an axis parallel to the borehole radiates detectable energy at frequencies $50 \leq f(t) \leq 350$ Hz. With small uniform displacement $u_0 \approx 1\ \mu$m, the DOV distributes fluid accelerations $a(t) = u_0\omega^2(t)$ of magnitude ≈0.1 g to ≈4 g over 4–5 s intervals. The simple, low-amplitude mechanics of DOV weight-spinning and acoustic force coupling to the borehole fluid are essentially linear, helping to produce stable correlation wavelets. Because the DOV is mechanically simple and coupled acoustically rather than dynamically to the rockmass, and because the DOV signal is a correlation wavelet smoothed over the irregularities of mechanical motion, DOV source signals can be highly reproducible. Also, the radial nature of DOV motion does not excite significant axially propagating tube waves in the source borehole fluid.

We describe DOV sourcing mechanics in Sections 2–3 based on acoustic and seismic radiation data recorded, respectively, in open water and crosswell geometries. The data are accurately described by two compatible mechanical-equivalence source models. The open-water radiation model derives from the exact physics of acoustic radiation of a rotating point force in an unbounded acoustic medium. The appropriate mechanical model for open-water pressure data is a monopole source with $1/r$ geometric scaling scaled by an effective source dimension determined by DOV parameters. A dipole-source component to DOV source action is clearly ruled out by the open-water acoustic data. The borehole seismic radiation model is an empirical kinematic description in which DOV dynamics are limited to pressure wave production within a borehole fluid, followed by kinematic conversion to seismic waves at the borehole wall. The amplitude and spectrum of crosswell seismic data are consistent with the geometrically reasonable picture of the source acoustic wave propagating in the borehole fluid as if diffracted from an aperture with the axial cross-section of the DOV. The DOV pressure wave produces seismic *P*- and *S*-wave waves at the wellbore. The acoustic and seismic radiation models are physically compatible in the sense that the effective dynamic DOV source dimension is smaller than a borehole radius. The physical parameters of the acoustic and seismic radiation models are fully determined, and model predictions agree well with field observation without adjustable parameters.

In Section 4 we address claims that acoustic action in a borehole fluid creates shear tractions in the surrounding rockmass and hence radiates primary *S* waves. The Section 2 evidence for monopole rather than dipole sourcing in DOV open-water acoustic data eliminates this claim. However, we make two further observations in this matter. First, the 2-D velocity field of a long cylinder along the z-axis moving along the x-axis in an acoustic medium is formally symmetric in interchange of $-x$ and $+x$ and, therefore, formally cannot have a significant dipole acoustic moment. Second, DOV data acquired with sensors and source at small offsets in the same borehole show no evidence for primary *S* waves propagating along the borehole axis (at high angles to the plane of the rotating point force where primary *S*-wave waves are most expected).

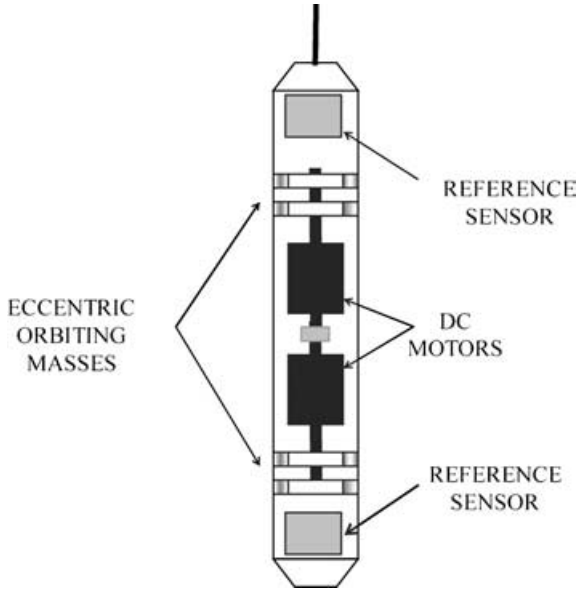

Figure 1. Schematic of direct-current-drive DOV. Motors spin the eccentrically weighted masses at increasing frequencies from standstill (0 Hz) to 350 Hz. The centrifugal force of the spinning eccentric masses displace the DOV sonde ≈1 μm in the instantaneous direction of the mass imbalance, initiating an acoustic wave in the borehole fluid. The acoustic wave front travels radially to the borehole wall to exit as seismic waves. The 5 s swept-frequency seismic wave train recorded by crosswell geophones is compacted to a ≈7.5-ms-wide seismic wavelet by cross-correlation with the DOV velocity signal provided by the reference geophones.

DOV rotary correlation wavelets have time-symmetry and source orientation properties that impact DOV source-wavelet reproducibility and time-lapse seismic imaging. The features of the correlation wavelet are discussed in a companion paper Leary & Walter (2005).

2 DOV ACOUSTIC RADIATION

2.1 DOV physical characteristics

The DOV excites acoustic waves in a borehole fluid by mass acceleration against the fluid. Acceleration is created by a pair of unbalanced masses rotated about the DOV axis as sketched in Fig. 1; rotation masses are unbalanced by holes drilled near their circumference. Rotation systematically increases from a stationary state (0 Hz) to ≈350 Hz over an interval of 4–5 s. DOV motion described here is sensed by orthogonal horizontal monitor geophones. Monitor signals are correlated with sensor motion recorded in offset boreholes. As rotary motion phase is more important for correlation and less predictable than motion amplitude, current DOV models substitute the continuous geophone monitor signal with phase monitor impulse signal. Table 1 outlines the physical parameters of the DOV supplying the data discussed herein.

DOV correlation wavelet production is illustrated in Fig. 2. The upper panel maps the time-progression of DOV frequencies recorded by monitor geophones as the rotational frequency moves through the effective minimum radiation frequency 50 Hz to peak at 325 Hz at time 4.5 s. After the peak frequency, the DOV mass spins down to below 50 Hz at ≈13 s. The lower panels show (left) the

Table 1. Direct-current-drive DOV physical parameters.

Parameter	Value
Power	300 W
Length × width	75 × 10 cm
Weight	11 kg
Max temperature	150°C
Depth range	0–5 km
Communications	7-conductor wireline
Operational frequency range	50–350 Hz
Correlation wavelet width	7.5 ms
Motion sensor	2 × 2 orthogonal horizontal geophones
Displacement amplitude	1 μm@50–350 Hz
Crosswell range:	
(i) 400 m in high-Q carbonates	(i) S/N $\gtrsim$ 3–5 per single sweep
(ii) 650–800 m in oilfield sediments	(ii) S/N $\gtrsim$ 5–10 per 15–25-sweep stack

unfiltered 7.5-ms-wide normalized auto-correlation wavelet of the DOV monitor signal and (right) a filtered and amplitude-compensated wavelet. Filtering removes high-frequency jitter and renders the correlation wavelet more compact where the rate of change of rotary frequency becomes too low to produce a compact correlation wavelet. Amplitude compensation removes low frequency trends in the DOV monitor sweep signal. Signal conditioning reduces auto-correlation wavelet side lobes relative to the main peak to yield a compact and easily interpreted signal wavelet, albeit at the loss of overall wavelet amplitude.

In discussing DOV mechanics, the correlation wavelet of Fig. 2 is often considered to be the primary physical phenomenon rather than being derived by cross-correlation of primary physical signals. We establish the physical basis for the source-sensor correlation. We first show that the DOV physical displacement is constant over the operational frequency range. Second, we consider the DOV acoustic wavefield produced in open water, and find the source is mechanically equivalent to a small rotating monopole force; the small size is compatible with acoustic action in a borehole fluid decoupled from the surrounding solid. Finally we consider the amplitude, spectrum and angular radiation pattern of crosswell seismic waves; the crosswell data are consistent with DOV generation of an acoustic diffraction wave front in the borehole fluid which then converts to seismic waves at the wellbore.

2.2 DOV constant-displacement acceleration

DOV acoustic radiation amplitude is proportional to centrifugal acceleration of the 11 kg mass distributed over a 1-m-long, 10-cm-diameter housing cylinder. Fig. 3 (left) shows the mean DOV velocity amplitude envelope for 15 sweeps recorded by two source monitor geophones. Each frequency sweep involves 4.5 s of powered up-sweep to 300 Hz followed by 10 s of unpowered down-sweep. The average DOV displacement spectra shown in Fig. 3 (right) are essentially uniform of order $u(f) \approx 1$ μm over the operational frequency range.

The source-monitor data ensemble behind Fig. 3 was recorded at 15 source levels at 5 m spacing over a 75 m borehole interval in oilfield sediments. The mean slopes of the 15 source displacement wave train spectra are -0.08 ± 0.03 and -0.13 ± 0.03, respectively, for the two source monitors. The displacement amplitude of the DOV is determined from the peak amplitude of $\approx$25 mV at 325 Hz, $u_0 \approx (25\ \text{mV})/(150\ \text{mV/cm s}^{-1})/(2\pi 325) \approx 8\ 10^{-5}$ cm $\approx$ 0.8 μm. The source spectra present no evidence for acceleration amplitude irregularities that might be ascribed to mechanical impedance complications introduced by the presence of a solid

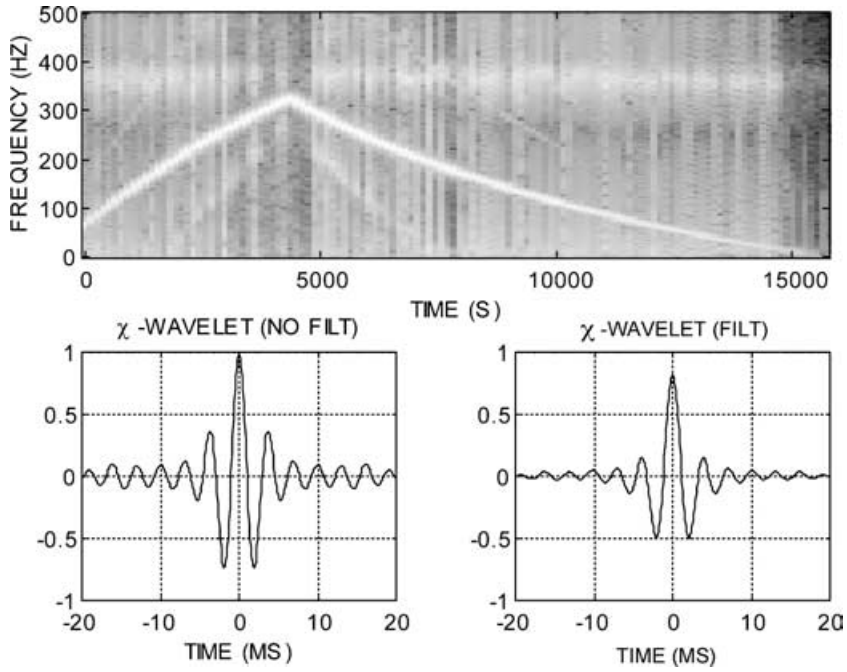

Figure 2. (Top) Spectrogram of DOV sweep monitor amplitude displayed in time and frequency; total sweep time is 16 s and highest sweep frequency is 350 Hz. The logarithm of the sweep function spectral amplitudes are coded by shade; light shades = high amplitude, dark shades = low amplitude. (Bottom) Unprocessed DOV correlation wavelets (left) and processed DOV monitor geophone (right). Wavelet processing included filter-limiting peak frequencies from 350 to 325 Hz and source-monitor amplitude compensation to reduce side-lobe amplitudes. The width of the correlation pulse is 7.5 ms.

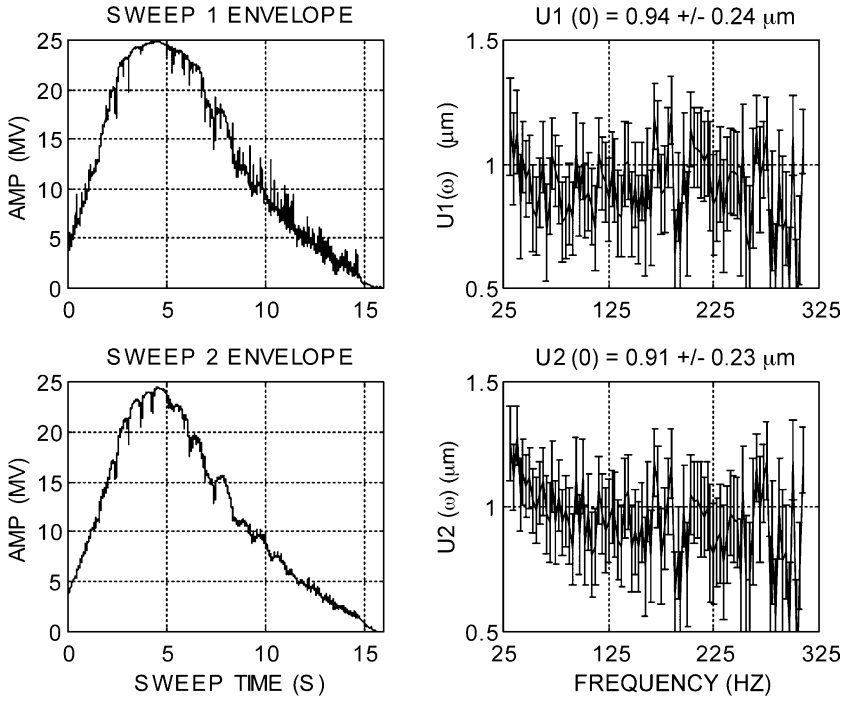

Figure 3. Mean DOV frequency-sweep monitor voltage envelopes (left) and mean displacement spectra (right) of DOV sweeps measured by the two orthogonal monitor geophones for 15-sweep stacks recorded at 20 × 5 m intervals in the source well. The DOV sweep is powered from 0 to 4.5 s and unpowered from 4.5 to 15 s. The DOV mass displacement in the borehole fluid is constant at ≈1 micron throughout the range of radiated frequencies.

enclosing the borehole fluid. For application to borehole operations, Fig. 3 data indicate that DOV seismic radiation can be modelled as a source with fixed displacement amplitude.

2.3 DOV as a point-force radiator in an unbounded acoustic medium

A DOV deployed in open water permits free sensor coverage relative to the source. Acoustic pressure data for complete angular sensor coverage can be acquired for the scale range of radii greater than the DOV characteristic physical dimension $\sqrt{2a\ell} \approx 30$ cm and less than the operational radiation wavelengths $\lambda \approx 5$–30 m. In this range of radii, the angular properties of the source pressure field define the DOV effective source type.

The simplest source type is a point force. A point force acting with time-function $F_0(t)$ along the x-axis in an acoustic medium produces a propagating pressure wave with displacement potential (Aki & Richards 1980),

$$\varphi(\boldsymbol{x}, t) = -1/(4\pi\rho)\, \partial_x(1/r) \int_0^{r/\alpha} d\tau\, \tau F_0(t-\tau). \quad (1)$$

Appendix A derives the acoustic displacement field $u_i(r)$ for a point force of constant displacement u_0, instantaneous frequency f and spatial frequency $k = 2\pi f/\alpha$ in a uniform acoustic medium of wave speed α. The acoustic field scales geometrically with radius as $1/r$ with a minor component of higher order term scaling as $1/r^3$,

$$u_i(r, t) = u_0 \gamma_i \gamma_x R_1/r[1 - [(1 + ikr) - \exp(ikr)](kr)^{-2}] \times \exp[i(\omega t - kr)]. \quad (2)$$

The angular pressure field is cylindrically symmetric with a lobular distribution determined by direction cosine γ_x for an instantaneous x-axis in the plane of the rotating point force. Acoustic radiation is maximum in the plane of rotation and null normal to the rotation plane. The acoustic radiation amplitude is scaled by the DOV equivalent mechanical radius $R_1 = \pi^2 \rho_{\rm dov}/\rho a^2 \ell/\lambda^2 \approx 1$ mm fixed by the physical dimensions DOV radius $a \approx 5$ cm and length $\ell \approx 1$ m, and acoustic radiation wavelength $\lambda = \alpha/f \approx 10$ m. At offsets small compared with the radiation wavelength, $r^3 \ll (\lambda/2\pi)^3$, eq. (2) reduces to

$$u_i(r, t) \approx 1/2 u_0 \gamma_i \gamma_1 R_1/r \exp[i(\omega t - kr)]. \quad (3)$$

In an unbounded acoustic medium, pressure $P(r)$ is related to the acoustic particle velocity by

$$\partial_t P(r, t) = -\rho\alpha^2 \partial_i v_i(r, t) = -\rho\alpha^2 \partial_t [\partial_x u_x(r, t) + \partial_z u_z(r, t)]. \quad (4)$$

For radii close to the DOV relative to the acoustic wavelength for frequency ω, eq. (3) substituted into eq. (4) gives the model pressure field as a function of position $[x, 0, z]$,

$$P(r, \omega) \approx -u_0 \rho\alpha^2 R_1 \{\partial_x [x^2 \exp(-ikr)/r^3] + \partial_z [xz \exp(-ikr)/r^3]\} \approx i\gamma_1 \rho u_0 \omega^2 R_1 \exp(-ikr)/(kr). \quad (5)$$

2.4 Observation of DOV acoustic radiation in open water

To test the rotating horizontal point-force model of DOV acoustic radiation eqs (1)–(5), a DOV was suspended from the centre of a floating platform at 15 m depth in 35-m-deep open water. DOV signals were recorded by a hydrophone successively located at the nodes of vertical grid passing through the axis of the suspended DOV. A total of $9 \times 4 = 36$ grid nodes were spaced at m-increments $z = [-4, \ldots, +4]$ m relative to the DOV at horizontal offsets x = [40, 80, 165, 300] cm from the DOV. Eq. (5) gives the model pressure field $P(x, z)$ as a function of hydrophone grid coordinates $[x, 0, z]$. Fig. 4 shows the *relative* amplitudes of observed and model wavelet pairs. The position of each observed/model wavelet pair is keyed to the sensor position in the 9 × 4 grid. For visual clarity, each

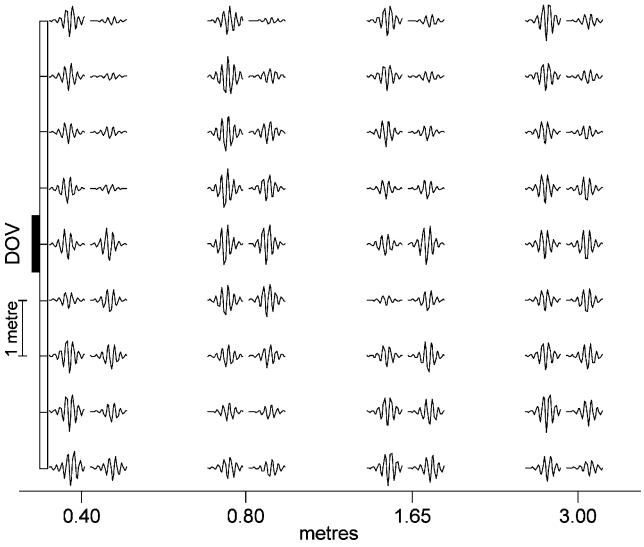

Figure 4. A 9 × 4 grid of observation/model DOV wavelet pairs. Each subplot pairs an observed wavelet (left) with a model wavelet (right). To aid visual inspection, wavelet-pair amplitudes are scaled to available plot space; absolute wavelet-pair amplitudes vary by factor 50 over the sensor grid. Data/model agreement is denoted by similarity of plotted wavelet amplitudes. Grid vertical intervals are 1 m; grid horizontal intervals are 40, 80, 165 and 300 cm from the DOV at left; for clarity, subplot horizontal locations are exaggerated by factor 3 relative to vertical locations. Model amplitudes are computed from eq. (5) except as noted in the text for locations closest to the DOV.

wavelet pair is scaled to occupy the maximum plot space; the scale of the horizontal spacing is expanded by a factor 3 over the vertical spacing.

In Fig. 4, model and observation agree at each sensor location if the wavelet-pair amplitudes are the same. The absolute amplitudes of the wavelet pairs vary by a factor of 50, from a nominal ±1 for the wavelet at column 2/row 5 to a nominal ±0.02 for subplots corresponding to larger offsets (column 4) and higher polar angles (rows 1–2 and 8–9). Aside from the model wavelet at column 1/row 5, wavelet amplitudes are as observed or as modelled relative to the unit wavelets of column 2 and row 5. The column 1/row 5 model wavelet at the grid position nearest to the DOV is artificially down-scaled to a representative value since the model amplitude is unrealistically large at offsets small compared with the physical size of the DOV. The Fig. 4 data are for counter-clockwise (*ccw*) rotation; closely similar data are recorded for clockwise (*cw*) rotations.

From the close agreement between wave-pair amplitudes at each sensor grid position in Fig. 4, the rotating point-force source model provides a good match to observation. Claims have, however, been made for dipole action from the DOV in a borehole (see Section 4.2). Fig. 5 addresses these claims by comparing the acoustic data of Fig. 4 to a dipole-source model pressure field. Details of the dipole field are given in Appendix A. Fig. 5 shows visually that, by comparison with a monopole source model, a dipole-source model provides a poor fit to the acoustic wavefield data.

We can put a quantitative interpretation on the visual model fits of Figs 4 and 5 by estimating the observational error from the difference of clockwise and counter-clockwise data wavelets. Denoting model values, observational amplitudes and errors for the ith sensor as, respectively, M_i, O_i and E_i, the chi-square goodness-of-fit estimator for observed and model pressure fields is

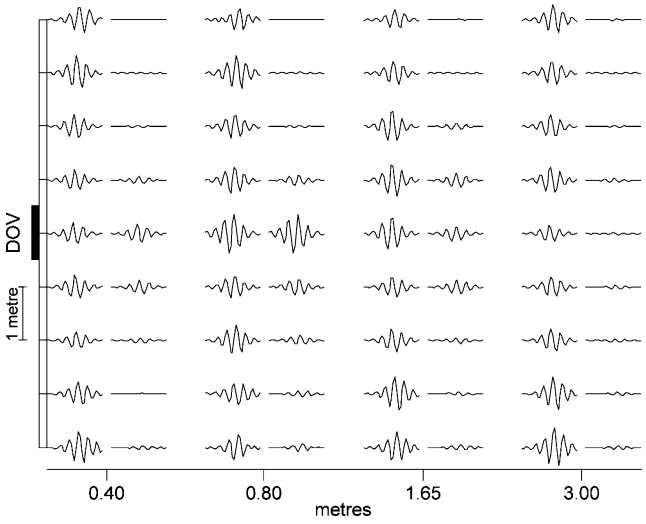

Figure 5. A 9 × 4 grid of observation-model DOV correlation wavelet pairs in the format of Fig. 4. Model wavelet amplitudes are computed for a dipole-source component for the DOV in open water. As shown by the relative amplitude mismatches between observation and model wavelet amplitudes, the $1/r^3$ scaling term of the model dipole source does not agree with observation.

$$\chi^2 = \sum_{i=1\ldots N} |O_i - M_i|^2 / E_i, \tag{6}$$

for index i taken over the $N = 29$ wavelet data at sensors which are not in the immediate vicinity of the DOV. While rigorous application of the chi-square test is associated with normal random distributions for O_i, M_i, and E_i, eq. (6) allows comparison of two models for data errors associated with non-systematic random fluctuations in background noise and sensor positioning (Press *et al.* 1992, Section 15.1). Chi-square estimator eq. (6) computed for the monopole and dipole DOV source hypotheses returns $\chi^2_{\text{monpole}} \approx 26$ and $\chi^2_{\text{dipole}} \approx 62$ for the $N = 29$ sensors excluding the 7 nearest to the normalization grid-point at column 2/row 5.

The chi-square value $\chi^2_{\text{monpole}} \approx 26$ meets the 'moderately good' fit criterion $\chi^2 \approx N = 29$, the number of independent tests (Press *et al.* 1992). Assuming that the estimated errors reasonably reflect non-systematic quasi-random fluctuations for 29 degrees of freedom, $\chi^2_{\text{monpole}} \approx 26$ corresponds to 50 per cent probability that the monopole model is compatible with observation. In contrast, the value $\chi^2_{\text{dipole}} \approx 62$ corresponds to a 0.01 per cent likelihood that a valid dipole hypothesis accidentally produces the observed deviation between model and data.

Fig. 4 indicates it is physically valid to model DOV as a rotating point force of effective mechanical size $R_1 \approx 1$ mm. This result indicates that the DOV sourcing action is effectively dynamically decoupled from the borehole wall. We thus examine DOV borehole seismic waves in terms of the kinematics of acoustic waves impinging on the borehole wall where they convert to *P* and *S* waves in the heterogeneous rockmass.

3 DOV BOREHOLE SEISMIC RADIATION

3.1 DOV seismic radiation: diffraction & normal-incidence of borehole acoustic wave

Fig. 6 shows a cross-section view of an empirical physical model of DOV borehole seismic radiation. The model focuses on the fluid gap

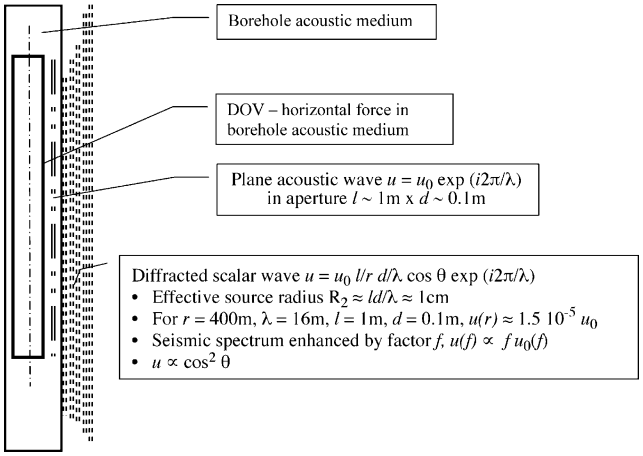

Figure 6. Cross-section of phenomenological model of DOV as rotating point force in an acoustic medium (borehole fluid). The axis of rotation is along the borehole axis. DOV instantaneous displacement normal to the borehole axis in the plane of the figure generates a horizontally moving plane acoustic wave in the gap between DOV and borehole wall. The plane acoustic wave is vertically truncated by the DOV length ℓ and horizontally truncated by the DOV diameter d normal to the plane of the figure, effecting acoustic diffraction from a planar slit of dimension $\ell \times d$. Seismic waves are generated by acoustic wave conversion at the borehole wall where DOV radiation and diffraction and conversion processes contribute a net seismic amplitude angular factor $\approx \cos^2\theta$ relative to the plane of rotation. Due to the source geometry and the source acoustic field, there is little excitation of axial pressure waves (tube waves).

between the DOV and the borehole wall. For a gap typically much smaller than the radial and axial dimensions of the DOV, acoustic waves reaching the borehole wall cannot differ significantly from the displacement motion of a plane wave exiting from a slit of cross-sectional area of the DOV. Such an acoustic wave front is equivalent to diffraction at a slit with the height and width of the DOV, as pictured in Fig. 6.

The amplitude, angular dependence and spectral form of scalar radiation emerging from a slit is described by Kirchhoff diffraction. From the derivation of Appendix B, for wavelength λ and offset r large compared with slit dimensions ℓ and d, the diffraction acoustic wavefield $u(\boldsymbol{r})$ at point $\boldsymbol{r} = r(\cos\theta, 0, \sin\theta)$ has amplitude and phase

$$u(r) \approx u_0 \ell d / r\lambda \cos\theta \exp(ikr). \qquad (7)$$

The actual picture of seismic sourcing is complicated by DOV acoustic wave conversion to seismic waves at the borehole wall in heterogeneous rock. Due to rock heterogeneity, converted S waves tend to be polarized both parallel and transverse to the borehole axis. Field data show, however, that eq. (7) provides a satisfactory empirical description of DOV crosswell wavelet amplitude, spectrum and radiation angular dependence.

3.2 DOV crosswell seismic wavefield amplitudes

For $\ell \approx 1$ m, $d \approx 0.1$ m, $r \approx 400$ m and $\lambda \approx 4000$ ms^{-1}/250 Hz = 16 m, eq. (7) gives the ratio of far-field displacement amplitude to source displacement amplitude as $u(r)/u_0 \approx 1.5\,10^{-5}$. Crosswell seismic motion data recorded at 405 m offset in high-Q carbonate rock validate the predicted diffraction process ratio. Fig. 7 shows P- and S-wave common-sensor gathers recorded at two of 10 levels in the reservoir. Each gather comprises sensor records for a single DOV sweep taken at 41 source depths in 6-m increments over a 240 m range of well depth. For source and sensor motion recorded in millivolts, the mean correlated source wavelet for the 10 gathers has amplitude $6 \pm 1\,10^6$ and the mean maximum correlated sensor wavelet has amplitude 55 ± 13. The ratio of mean maximum sensor amplitude to mean source amplitude is $0.9 \pm 0.2\ 10^{-5}$.

The diffraction model seismic displacement amplitude ratio $(u(r)/u_0)_{\rm mod} \approx 1.5\,10^{-5}$ agrees with the observed the seismic displacement amplitude ratio $(u(r)/u_0)_{\rm obs} \approx 0.9 \pm 0.2\,10^{-5}$ to within 50 per cent. This level of amplitude agreement with no adjustable parameters supports the hypothesis that the DOV operates in a borehole with source equivalent dimension of order $R_2 \approx d\ell/\lambda \approx 1$ cm given by the diffraction process expression eq. (7).

In terms of the diffraction model, the 50 per cent seismic wave amplitude discrepancy can be discussed in terms of plausible physical details omitted from model. Missing physical details include acoustic wave conversion to P waves, the generation of S-wave motion from the primary P wave, attenuation due to absorption of seismic energy and the effects of medium heterogeneity including wave energy channelling in the layered reservoir formation.

The amplitude effect of acoustic plane wave conversion to seismic waves at the wellbore can be estimated from the impedance relation for normal incidence reflection and transmission coefficients, $t = 1 + c$, and energy conservation for impedance $I = \rho\,\alpha$, $I_a = c^2\, I_a + t I_e$ (Claerbout 1976). For $I_a = (1$ g cc$^{-1})$ $(1.5$ m ms$^{-1})$ and $I_a = (2$ g cc$^{-1})(4$ m ms$^{-1})$, $t = 2I_a/(I_a + I_e) = 2(1.5)/(1.5 + 8) = 3/9.5 \approx 1/3$ in energy or $1/\sqrt{3}$ in amplitude. Reducing amplitude (eq. 7) by the $1/\sqrt{3}$ conversion factor, $1.5/\sqrt{3}\,10^{-5} = 0.87\,10^{-5}$, gives close agreement between eq. (7) and Fig. 7 data.

It is evident from Fig. 7, however, that heterogeneity of the rock medium can distort observed amplitudes from the predictions for a uniform medium. For instance, to the extent that normally incident plane wave conversion describes the acoustic–seismic interface, no S waves are produced. Observed S-wave production is, therefore, due to interaction of primary converted P waves with the layered formations, which also leads to P- and S-wave energy channelling in fast and slow layers. The combined effects of amplitude reduction to generate S-wave motion and amplitude enhancement due to energy channelling do not allow a simple model to be quantitatively precise.

Seismic attenuation due to internal friction parametrized by Q also plays a role in the seismic wavelet amplitudes. However, in contrast with most oilfield sedimentary rock, the amplitude effect of Q is limited for the reef carbonate crosswell data of Figs 7–9. At the appropriate crosswell seismic parameters $r \approx 400$ m and $\lambda = \alpha/f \approx 4000$ ms^{-1}/250 Hz = 16 m, a value of $Q \approx 200$ reduces the wavelet amplitude on the order of 30 per cent ($e^{-\pi fr/\alpha Q} = 0.67$). Observation rules out values of Q significantly lower than, say, 200. First, unusually for crosswell seismic data, uncorrelated sensor motion can be detected for the carbonate formation data. Sensor motion spectrograms (equivalent to the Fig. 2 source motion spectrogram) show uncorrelated single-sweep energy above background seismic noise, with the single-sweep sensor spectrograms showing significant energy at peak frequencies 250–300 Hz. Second, for correlated wavelets, Q values significantly lower than 200 would distort the power-law spectral trend predicted by eq. (7) and seen in Fig. 8.

While some uncertainty on the details of agreement between observation and diffraction model expression (eq. 7) remains, the essential conclusion is that Fig. 7 crosswell seismic data from a high-Q carbonate formation provide solid evidence for an effective DOV source dimension of order $R_2 \approx 1$ cm. Values of this order meet the condition $R_2 \ll R_{\rm borehole}$ for effective decoupling of DOV source action from the borehole wall.

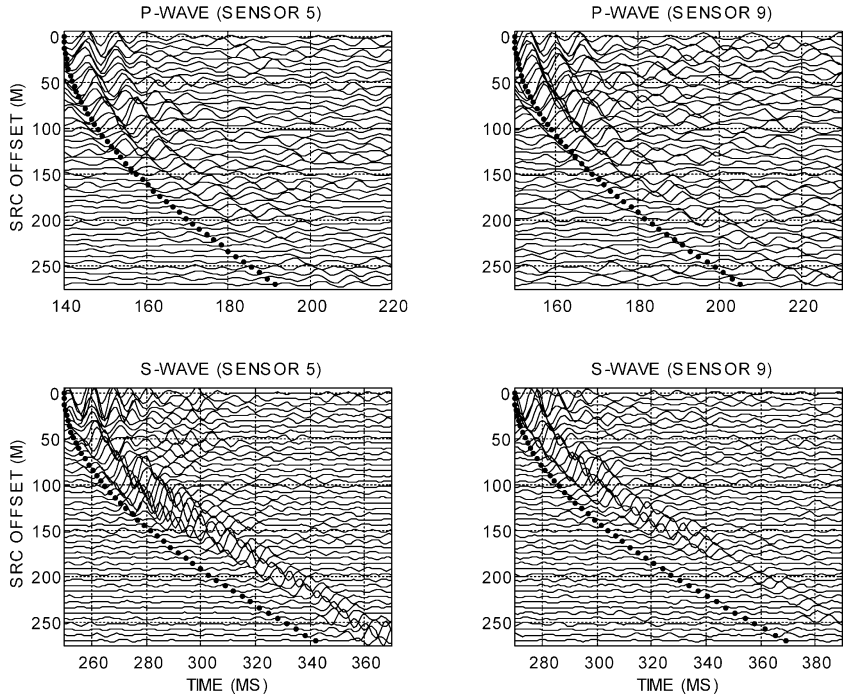

Figure 7. Sample crosswell seismic common sensor gathers of *P* and *S*-motion for single DOV sweeps at 405 m offset in a high-Q carbonate reservoir. Peak amplitudes of the correlated sensor motion for each of 10 gathers average 55 ± 13 relative to the mean source wavelet amplitude $6 \pm 1\ 10^6$; the ratio is $0.9 \pm 0.2\ 10^{-5}$. Dots denote traveltimes for uniform medium with mean sonic-log velocity.

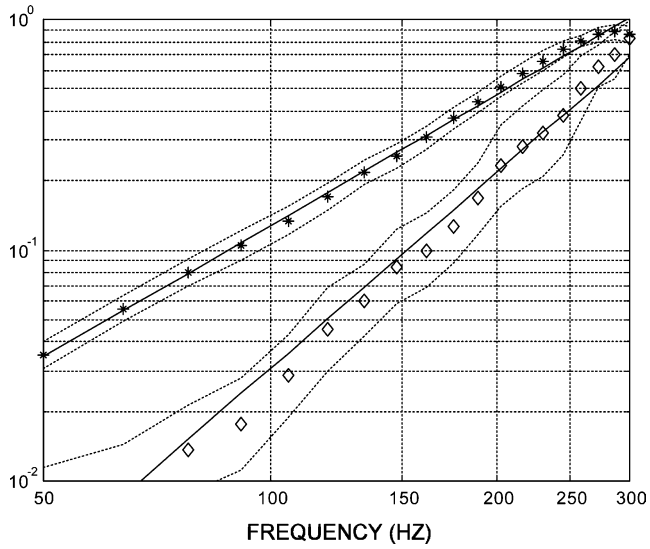

Figure 8. Comparison of DOV source correlation wavelet mean spectra (asterisks) with crosswell seismic sensor correlation wavelet mean spectra (diamonds) from field data recorded at 405 m offset in oilfield carbonates (Fig. 7). Solid lines are power-law fits to the spectral trends of form f^{β}, where β is the slope of the trend in a log–log plot. Dashed lines represent 1-standard deviation statistical error-bars on the spectral amplitudes. The source wavelet spectral trend gives $\beta = 1.88 \pm 0.12$ for the sample of 40 DOV source wavelets; the sensor wavelet spectral trend gives $\beta = 2.82 \pm 0.35$ for the sample of 127 largest wavelets in 10-gather ensemble of 400 sensor wavelets. The slope of the source spectrum is expected from the auto-correlation of a velocity sensor recording a frequency sweep. The sensor spectrum is consistent with linear frequency enhancement of the source spectrum given by the diffraction model (7).

3.3 DOV crosswell seismic sensor spectra

Diffraction radiation amplitudes (eq. 7) depend linearly on the wave frequency as $u(r) \approx (\ell d / r\alpha) u_0 f$. Crosswell seismic sensor spectral amplitudes are hence expected to be linearly enhanced in frequency factor f relative to DOV source spectra. Fig. 8 shows that the source wavelet mean spectrum (asterisks) and sensor wavelet mean spectrum (diamonds) are consistent with the diffraction picture of DOV borehole operation.

In Fig. 8 the observed source mean spectrum has power-law trend with slope 1.88 ± 0.12, denoting a spectrum essentially proportional to f^2. A constant spectral power law with exponent near 2 is expected for the DOV auto-correlation wavelet derived from a monitor geophone responding to rotary frequency modulation with constant displacement u_0 (one factor f due to geophone output proportional to angular velocity, the second factor of f due to the quadratic nature of the auto-correlation function). At the same time, the sensor wavelet mean spectrum has slope 2.82 ± 0.35, corresponding to frequency enhancement of the source spectrum by factor f^{β}, $\beta \approx 0.94 \pm 0.37$. The observed frequency enhancement is consistent with diffraction model (eq. 7) at a three-standard deviation level of significance. As observed in the previous section, this agreement rules out significant Q effects in the carbonate data. We note further that the stable source wavelet spectral slope 1.88 ± 0.12 is determined over 40 source levels at 6 m intervals for 240 m of borehole. While the Fig. 7 sensor gathers give evidence for a layered borehole medium, the source spectrum is essentially constant throughout the range of source well depths, again arguing for essential decoupling of the source motion from the borehole environment.

3.4 DOV crosswell seismic radiation pattern

An angular amplitude trend is seen in the DOV seismic radiation of Fig. 7. The angular amplitude trend can be parametrized by

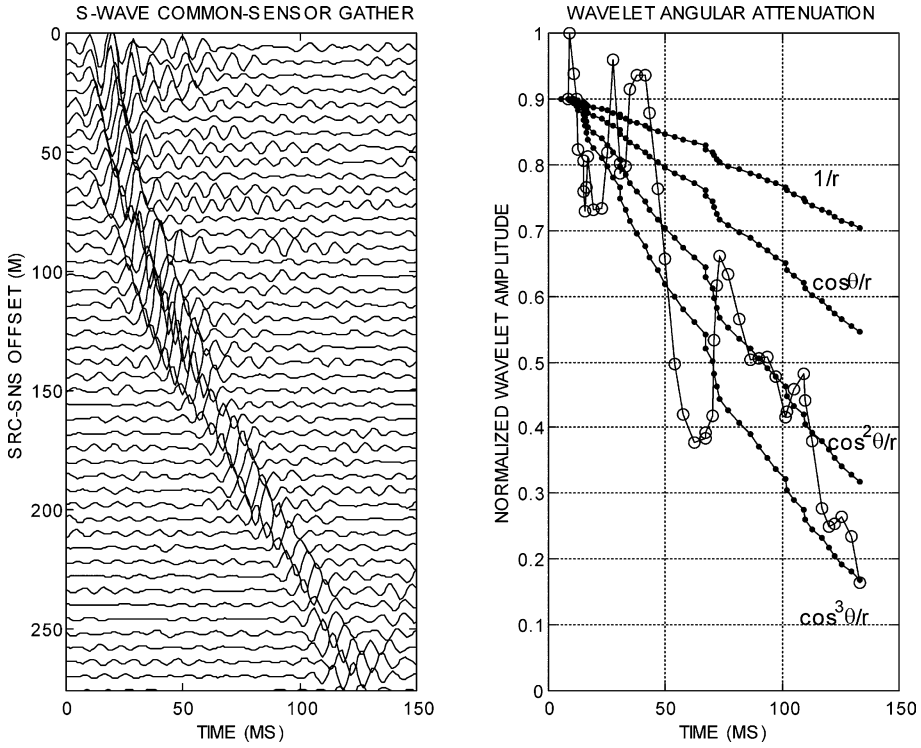

Figure 9. (Left) Amplitude decay with crosswell ray path angle increasing from 0° to 30°. (Right) Quantified amplitude trend of crosswell sensor wavelet amplitude (circles) compared with amplitude decay trends (dots) comprising geometric attenuation $1/r$ weighted by powers of angular radiation pattern $\cos^n\theta, n = 0, 1, 2, 3$.

angle θ between the source-sensor ray path and the horizontal plane. *P*- and *S*-wave amplitudes in the Fig. 7 gathers are largest for near-horizontal ray paths ($\theta \approx 0$), and fall-off as the source moves to larger vertical offsets ($\theta \rightarrow 30^\circ = atan(240/405)$ for 240 m source-sensor vertical offset and 405 m horizontal offset). The diffraction model of DOV radiation (eq. 7) predicts that wavelet amplitudes fall-off as $\cos\theta$. The effect of an additional $\cos\theta$ factor may be expected from the kinetics of a normally incident *P*-wave point force on an elastic medium (Waters 1981).

Fig. 9 compares the angular amplitude decay of a representative Fig. 7 seismic wavelet gather with angular amplitude decay from geometric attenuation weighted by angular factors in the cosine of the ray path angle, $\cos^n\theta, n = 0, 1, 2, 3$. The observed mean amplitude trend shown in Fig. 9 (left) is observed over 40 source depths at 6 m intervals covering ray path angles 0° to 30°. Fig. 9 (right) compared the quantified wavelet angular amplitude trend with the trend of the geometric factor $1/r$ weighted by factors of $\cos\theta$ expected from the action of diffraction model (eq. 7), conversion of normal pressure waves to seismic waves (Waters 1981), and the effect of channelling in layered media. The data of Fig. 9 are consistent with at least two source radiation angular factors of $\cos\theta$ in addition to $1/r$ geometric attenuation. As with the Fig. 7 absolute amplitude data, the diffraction model agrees with observation in spite of the complexity of the acoustic-to-seismic radiation process in a heterogeneous medium. The observed angular radiation pattern is consistent with acoustic radiation in the borehole fluid converting to primary *P* waves and converted *S* waves at the wellbore. The angular data give no support for the production of primary *S* waves though shear distortion of the elastic medium.

The general features of crosswell seismic data recorded at 405 m offsets by 10 sensors for 40 source levels at 6 m intervals in high-*Q* carbonate reservoir rock agree with the simple diffraction model of DOV borehole seismic source mechanics expressed by eq. (7) and illustrated in Fig. 6. The agreement can be summarized by:

Parameter/value	Crosswell data in high-*Q* layered carbonate formation	Diffraction model with acoustic/seismic conversion
Absolute amplitude	$9 \pm 0.2\ 10^{-6}$	$9\ 10^{-6}$
Sensor/source spectral ratio	$f^{0.96\pm0.35}$	f^1
Angular aperture	$\cos^2\theta$	$\cos^2\theta$

Further quantification of the diffraction model can be pursued, but we note that the principle objective in understanding DOV source mechanics is testing the robustness of the claim that the effective mechanical source dimension of the DOV is small compared with a typical borehole radius. With a small mechanical dimension, the DOV is effectively mechanically decoupled from the borehole environment and hence is expected to be stable for sensitive repeat seismic sourcing required by time-lapse seismic imaging of geofluid reservoirs. Such decoupling is incompatible with the production of primary shear waves.

4 FURTHER EVIDENCE OF DOV KINEMATIC COUPLING

We have presented an observational basis for a kinematic model of DOV borehole seismic sourcing isolated from the complications of dynamic coupling to the surrounding rockmass. The kinematic

model is important because acoustic coupling of the DOV mechanical action to the seismic field is both operationally safe and inherently stable. Operational safety of a borehole seismic source with an essentially 1 km crosswell range enables effective crosswell seismic access to a large population of reservoir production wells, while source wavelet stability enables development of time-lapse seismic monitoring of reservoir production. As, however, DOV borehole sourcing action has not hitherto been regarded in purely kinematic terms, we discuss additional data in support of a predominately kinematic action for DOV action in boreholes. Leary & Walter (2005) further validate the kinematic model through detailed discussion of the kinematic phase relation between the source and crosswell seismic correlation wavelets.

4.1 DOV steady-state acoustic velocity field

In the immediate vicinity of a DOV operating at frequencies 50–350 Hz in a borehole fluid, the tool is effectively an infinite cylinder admitting of a 2-D potential description of the acoustic velocity field. The velocity field of steady-state motion for a cylinder in a fluid is incompatible with claims for a dipole-source component of DOV action in a borehole fluid (see Section 4.2).

At operating frequencies 50–350 Hz, the DOV moves at laminar flow speeds in water. At amplitude $u_0 \sim 10^{-6}$ m, the velocity at 200 Hz is $v \sim 400\pi u_0 \sim 10^{-3}$ m s^{-1}. The largest dimension of the DOV is its length $\ell \approx 1$ m. Water with kinematic viscosity $\eta \sim 1$ centistoke $= 10^{-6}$ m^2 s^{-1} and density 1 g cc^{-1} yields Reynolds numbers $Re = \ell v/\eta \approx 10^3$. Turbulent flow is associated with Reynolds numbers >6000–10 000. For velocities $10^{-3} \ll 1500$ m s^{-1}, the laminar acoustic wavefield is instantaneously established. Under these conditions, the DOV instantaneous acoustic velocity field $\mathbf{v}(r, \theta)$ derives (Appendix C) from the streamline velocity potential in the plane normal to a long cylinder radius $a = d/2$ moving with instantaneous velocity $v_0 = 2\pi f u_0$ determined by DOV displacement u_0 and frequency f. The resulting kinematic velocity field,

$$\mathbf{v}(r, \theta) = v_0 a^2/r^2[\cos 2\theta \boldsymbol{x} + \sin 2\theta \boldsymbol{y}], \tag{8}$$

with $r > a$ the radius vector and θ the radius angle relative to the direction of DOV displacement, is shown diagrammatically in Fig. 10.

The steady-state velocity field (eq. 8) formally models fluid motion in the vicinity of the DOV at field operating conditions. The velocity field is symmetric along the x-axis, $\theta = \pm 180^\circ$, ruling out by symmetry first-order dipole pressure. Moreover, the velocity field at $\theta = \pm 90^\circ$ cannot be construed to generate shear distortion of the borehole.

4.2 Claims for DOV primary *S*-wave radiation

Geophysical literature discussing the DOV or based on DOV data (Liu *et al.* 1991, 1993; Cole 1997; Daley & Cox 2001) suggests that an (unclamped) DOV operating in a borehole is a source of polarized *S* waves at radiating at high angles to the plane of DOV acceleration. The claim is that a DOV operating in a borehole fluid nonetheless radiates as if the point-force vector were in an elastic rather than in an acoustic medium. For instance, Cole (1997) characterizes the DOV as a 'dipole source' that 'produce[s] a radiation pattern the same as that produced by a similar source buried in the Earth'. The essence of this statement is that, by some form of dipole action within the borehole fluid, the DOV creates shear tractions in the rockmass so that a DOV in a borehole effectively radiates as if it were embedded

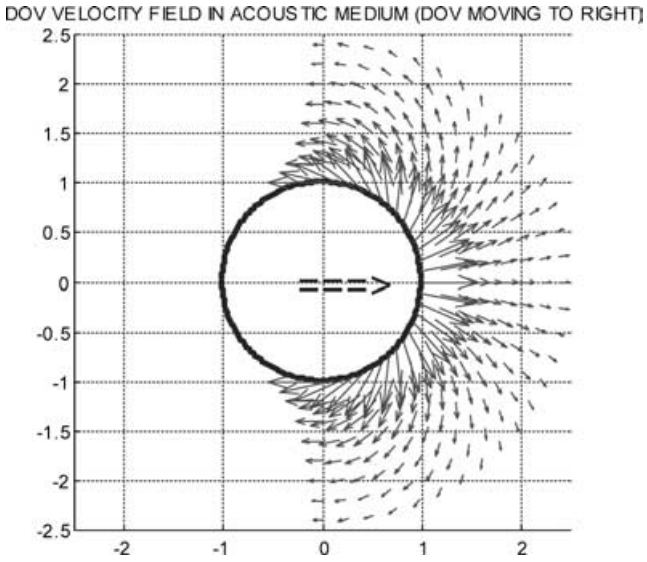

Figure 10. 2-D kinematic velocity field for a long rigid cylinder moving towards the right of the figure at right-angle to its axis of symmetry. The steady-state velocity field (eq. 8) is similar in amplitude and radial dependence to the static near-field of the dynamic DOV model eqs (2) and (3). The static laminar velocity field at right angles to the direction of motion is equal and opposite to the motion of the DOV, illustrating that instantaneous motion of the DOV in a fluid can not exert shear tractions on a borehole wall. The symmetry of the velocity field precludes the existence of a dipole moment to the DOV action.

in an elastic rather than an acoustic medium. We here discuss the evidence cited by the above authors in favour of DOV production of shear tractions in the rockmass and consequent primary shear wave radiation.

To connect this characterization of DOV borehole seismic waves more closely to statements of the other authors, we assume that the 'dipole' action of the DOV is equivalent to a horizontal point force elastically coupled to rock and instantaneously pointing along the x-axis at depth z in the Earth. In parallel with the acoustic *P*-wave model expression (A2) of Appendix A, a vibrating point force along the x-axis in an elastic medium generates primary (as opposed to converted) *S* waves with far-field behaviour

$$u_i^{ff}(r, t) = F_0(t - r/\beta)(4\pi\rho\beta^2)(\gamma_i\gamma_x - \delta_{ix})/r. \tag{9}$$

Since *P* waves have radial polarization γ_i, contraction $\gamma_i(\gamma_i\gamma_x - \delta_{ix}) = \gamma_i\gamma_i\,\gamma_x - \gamma_i\delta_{ix} = 1\gamma_x - \gamma_x = 0$ confirms the *S*-wave nature of the radiation (eq. 9). Consider now *P*- and *S*-wave polarizations for position vector $[x, 0, z]$ at high angles to the point force along the x-axis, $[x, 0, z] \rightarrow [0, 0, 1]$. This corresponds to observing the buried DOV from more or less directly above, that is, along the borehole axis if the DOV is suspended in a vertical borehole. While *P*-wave radiation with directionality $\gamma_i\gamma_x = [x^2/r^2, 0, xz/r^2]$ vanishes as the x-component of the position vector vanishes, *S*-wave radiation with polarization $(\gamma_i\gamma_x - \delta_{ix}) = [x^2/r^2 - 1, 0, xz/r^2] \rightarrow [-1, 0, 0]$ attains its largest amplitude along the borehole axis, at high angles to the horizontal plane in which the DOV point-force rotates.

Primary *S*-wave radiation at high angles to the plane of point-force rotation would be a desirable feature in a borehole seismic source. In the case of the DOV operating in a vertical borehole, as the source point-force vector rotates from the x-axis to the y-axis the primary *S*-wave polarization at high angles to the horizontal changes with the point-source vector, yielding (if the DOV acted as an elastic point shear force) a complete range of *S*-wave polarizations for vertical

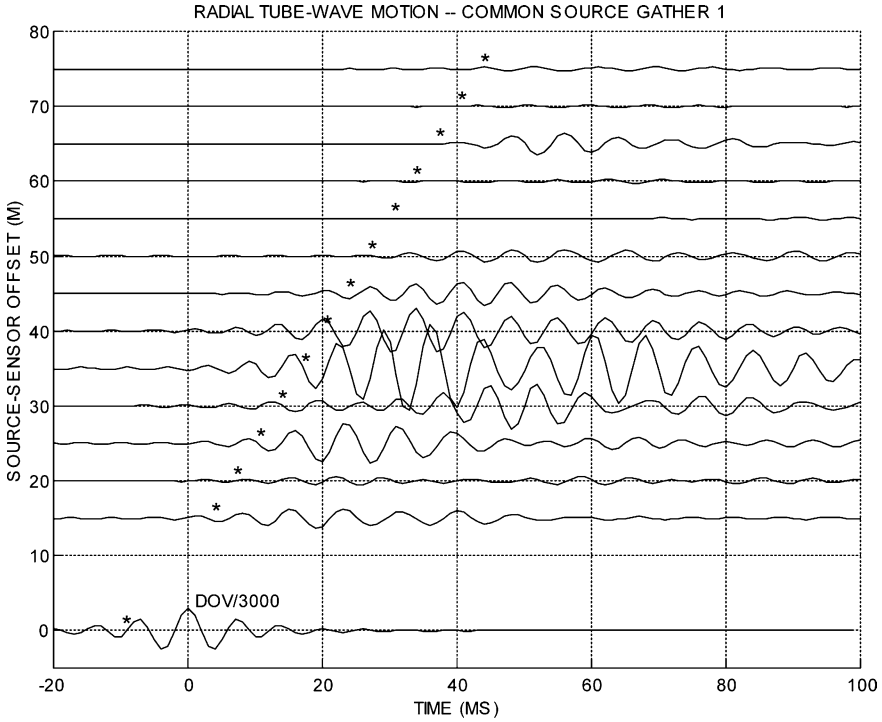

Figure 11. DOV-excited radial tube wave motion at 4 km depth in salt recorded by 13 clamped geophones at 5 m intervals 15–75 m above the DOV. The plot time-origin is fixed at the central peak of zero-phase source wavelet. Asterisks identify the observed motion as tube waves with characteristic 1.5 m ms^{-1} moveout along the array. The corresponding DOV wavelet shown at 0 m offset and labelled 'DOV/3000' is downscaled by factor 3000 relative to the scale of the tube wave amplitudes.

S-wave ray paths. Such notional primary radiation is termed by Daley & Cox (2001) 'circularly polarized waves', and conforms to the description of Liu *et al.* (1991, 1993) of the radiation expected from a DOV in a borehole-sourced RVSP experiment in fractured limestones. (It should be noted that notional primary 'circularly polarized' primary *S* waves occur only for sensors situated on or near the DOV rotation axis; at sensor locations off the DOV rotation axis, primary *S* waves are 'elliptically polarized', with the ellipse collapsing to a horizontal line for DOV crosswell data.)

According to the literature of which the present authors are aware, no primary evidence has been produced for DOV generation of *S* waves at high angles to the borehole radial plane. Daley & Cox (2001) present only crosswell data well using sensors at essentially 90° from the DOV rotation axis (in the plane of the rotating point force). Cole (1997) shows no data. Liu *et al.* (1993) present RVSP data having the correct observational geometry for recording high-angle primary shear waves but offer only the following statement in support of their observation [italics supplied]: 'The full-wave modelling . . . . *suggests* that this source yields impulsive *SH*- and *SV*-wave signals for nearly vertical ray paths *that can be modelled* synthetically using horizontal forces'.

If such radiation did exist, it should be straightforward to demonstrate the signal in a single borehole using a DOV operated on the same wireline as a string of sensors. Section 4.3 shows, instead, evidence that no primary *S*-wave radiation is recorded by sensors 15–75 m from the source at signal sensitivity of order 1 part in 10^5 of the primary DOV signal.

4.3 DOV tube waves and axially propagating body waves

Tube waves are axially propagating fluid pressure fronts trapped in the low-velocity channel of borehole fluid in a rock matrix. As energy propagating in a single dimension in a high-Q medium ($Q_{\text{water}} \approx 10^5$), tube waves do not decay geometrically or intrinsically with distance from the source, and hence can potentially interfere with seismic signals returning to wellbore sensors from the surrounding formation. DOV tube wave production is straightforward to observe by operating a DOV attached to a sensor string in a single well. Single-well data also determine the level at which the DOV can be suggested to mechanically shear the borehole formation to generate axially propagating *S* waves. Figs 11 and 12 and Table 2 summarize a suite of DOV single-well data acquired at 24 levels along a 1000 m well interval at 4 km depth in a Gulf of Mexico salt body. We can compare these data with single-well data acquired by Daley *et al.* (2003) using a powerful orbital vibrator at 600 m depths in poorly consolidated oilfield sediments (*S*-wave velocity $\approx$0.8 m ms^{-1}).

Fig. 11 shows a sample common-source gather of horizontal motion recorded by 13 sensors offset at 5 m intervals between 15 and 75 m from the DOV. Fig. 12 gathers mean amplitude envelopes computed for all 24 well observation depths. Tube wave maxima and upper limits on *P*- and *S*-wave motion are related to the DOV source wavelet amplitude in Table 2.

Since DOV seismic source radiation is primarily in the plane of DOV rotation, that is, normal to rather than along the borehole axis, DOV backscatter imaging data appear primarily as radial sensor motion. The radial component of tube wave noise is, therefore, more important for imaging than the axial component. Sample data in Fig. 11 calibrate the amplitudes of radial tube wave motion at successive 5 m well offsets relative to the scaled DOV monitor wavelet shown at zero offset. The tube wave is readily identified by its 1.5 m ms^{-1} moveout across the sensor array as indicated by asterisk-marked traveltimes. Tube wave amplitudes are at least three orders of magnitude smaller than the DOV source wavelet. There is no

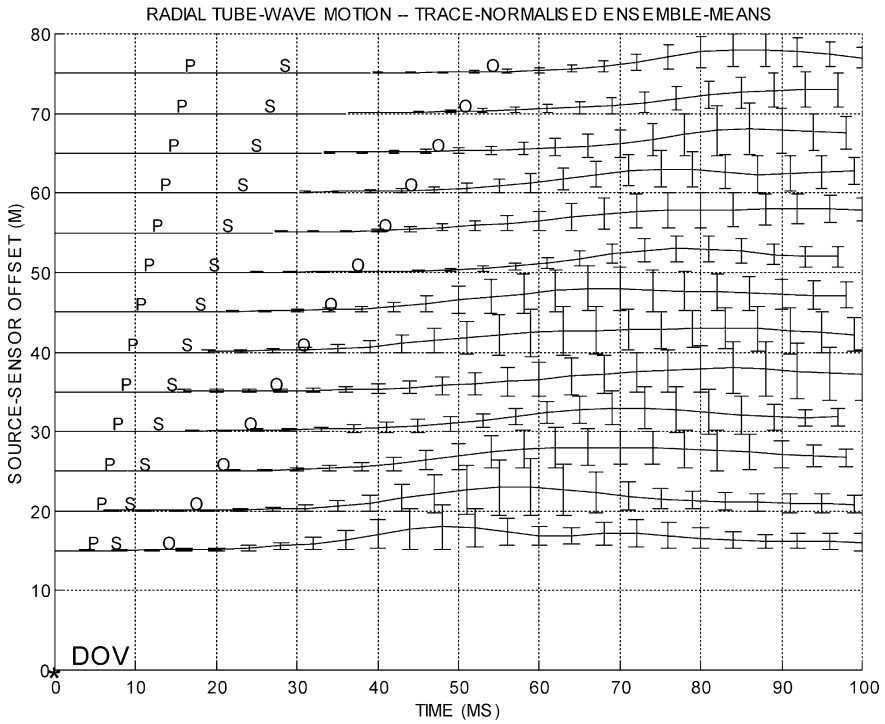

Figure 12. Trace-normalized tube-wave amplitude envelopes averaged over 24 common-source gathers recorded along the 1000 m well interval of Gulf of Mexico salt body. Mean tube-wave amplitude envelopes are of order 1000 times smaller than the DOV wavelet amplitude. Circles and letters '*P*' and '*S*' mark arrival times of, respectively, tube waves and axially propagating *P*- and *S* waves excited by DOV at zero offset in time and space. The traces show no motion in the *P*- and *S*-wave time windows at the level of 10 per cent of the smallest tube waves. Table 2 indicates that *P*- and *S*-wave amplitudes are at most of order 30 times smaller than tube wave amplitudes.

evidence of axially propagating *S*- or *P* waves in the time interval before tube wave arrivals.

Fig. 12 confirms the sampled amplitude systematics of Fig. 11. The trace-normalized mean amplitude envelopes computed over all 24 observation depths also puts upper limits on the size of axially propagating *P* and *S* waves at less than 10 per cent of the smallest tube wave amplitudes. The observed limit of DOV-excited body wave motion at the expected *P* and *S* arrival times is quantified in Table 2 at 2–3 per cent of the smallest tube wave envelope maxima, indicating an overall body wave limit of order 10^{-5} to 10^{-6} of the DOV wavelet magnitude for borehole operations in a homogeneous medium such as salt.

In Fig. 11, tube wave amplitudes are seen to decrease markedly with offset due to acoustic scattering at the bulky 1/2-m-long clamped sensor modules occupying 40–50 per cent of the wellbore. Daley *et al.* (2003) observe a similar tube wave amplitude reduction using an acoustic baffle between the DOV and the sensor string. As quantified in Table 2, when tube wave energy is scattered by elements of the borehole sensor string, the residual tube wave noise can be a factor 10^4 smaller than the radial acoustic signal.

Small tube wave amplitudes are not surprising given that the DOV does not excite volume changes within the fluid. Borehole sources associated with strong tube waves involve volume changes within the fluid, as in the explosive gas phases of the airgun and underwater sparker, and the solid-state volume deformations of magnetostrictive materials and piezocrystals as observed by Daley *et al.* (2003). However, the remarkably low levels of observed DOV-excited tube and body waves in Figs 11 and 12, 1 part in 10^4 for tube waves and 1 part in 10^5–10^6 for body waves, suggest additional contributions from the mechanics of a rotating point force in an acoustic medium and from the radial plane acoustic wave observed via diffraction effects in the converted seismic wavefield.

Axially propagating body waves generated by an acoustic borehole source are, of course, readily observed at higher frequencies. Sonic well logging tools operating at frequencies of tens of kilohertz routinely register refracted body waves at 1–3 m source-sensor offsets. Daley *et al.* (2003) identify low-amplitude *P* waves in advance of tube waves for a scaled-up version of sonic logging tool comprising a 2 kHz piezoelectric source with sensors at 10–30 m offsets. In direct comparison with the data of Figs 11 and 12, Daley *et al.* (2003) record low-amplitude *S* waves and barely detect *P* waves for a 50–350 Hz orbital vibrator in place of the piezoelectric source.

Sonic tool body waves have, however, wavelengths of order 10 cm and hence are produced by geometric ray refraction within the damage halo of the borehole rather than by shear distortions of the borehole. The metre-wavelength piezoelectric source data of Daley *et al.* (2003) respond weakly to the borehole damage halo but at the same time do not produce clearly identifiable *S* waves and hence do not offer evidence for primary shear distortion of the borehole medium. The marginal *P* waves and larger *S* waves observed by Daley *et al.* (2003) in orbital vibrator source data conform most closely to the expectations for waves excited by primary shear distortions of the borehole medium. However, such *S* waves are expected from *P*-to-*S* scattering in a heterogeneous medium and do not automatically signify primary shear distortion of the borehole medium. In this regard, the absence of *S* waves in Figs 11 and 12 could be as much due to the relative homogeneity of salt as a borehole host medium as to lack of primary shear distortion.

We also note that the *S* waves identified by Daley *et al.* (2003) are smaller than the tube waves, and can be seen only if the tube waves

Table 2. Mean and standard deviations for maximum amplitude horizontal wave motion recorded by 13-sensor array at 24 depths along a 1000 m well interval. Given amplitudes are normalized to a unit amplitude DOV wavelet. Column 1 gives sensor offsets from DOV; columns 2–4 give maximum mean amplitudes in time intervals for, respectively, tube waves (TW), *P* waves (*P*), and *S* waves (*S*) as marked for each sensor in Fig. 12.

Sensor offset (m)	Mean TW ($\times 10^{-4}$)	Amplitude mean *P* wave ($\times 10^{-6}$)	Amplitude mean *S* wave ($\times 10^{-6}$)
75	0.8 ± 0.4	1.6 ± 0.7	1.6 ± 0.7
70	1.3 ± 0.8	1.9 ± 1.1	2.0 ± 1.0
65	1.3 ± 0.8	1.6 ± 1.6	1.8 ± 1.7
60	1.0 ± 0.5	1.8 ± 0.9	1.9 ± 1.0
55	0.9 ± 0.3	1.5 ± 1.1	1.7 ± 1.4
50	2 ± 1	2.8 ± 1.4	3.3 ± 1.7
45	2 ± 1	4.0 ± 3.2	5.0 ± 4.0
40	3 ± 2	16 ± 8	10 ± 10
35	6 ± 4	6 ± 3	23 ± 18
30	3 ± 2	11 ± 7	14 ± 12
25	5 ± 3	25 ± 17	24 ± 19
20	9 ± 5	38 ± 27	100 ± 83
15	6 ± 4	29 ± 12	152 ± 123

are scattered by an acoustic baffle out of the fluid column before they reach the sensor string. Even if the *S* waves are in part due to primary shear distortion of the borehole medium, they are orders of magnitude smaller than the primary source wave generated by the DOV and hence appear to offer virtually no prospect for exploring significant volumes of reservoir media surrounding the observation borehole.

5 CONCLUSIONS

The DOV is a compact, robust, low-power, environmentally benign swept-frequency acoustic energy source that operates on a standard 7-conductor wireline up to 150°C temperatures and 5 km depths. Acoustic and seismic data point to DOV borehole seismic sourcing as originating from linear acoustic coupling to the borehole fluid and subsequent kinematic wave conversion at the wellbore. A simple empirical model of acoustic wave diffraction in the borehole fluid satisfactorily predicts the amplitude, spectrum and angular aperture of crosswell seismic waves. Agreement between data and model strengthens our hypothesis that the DOV is dynamically independent of the borehole wall, with the implication that DOV-generated borehole seismic wavelets gain stability from uniform fluid conditions rather than being subject to heterogeneity of borehole geometry and physical properties.

Our observations and modelling support the following general physical characteristics of DOV borehole seismic sourcing:

(i) The DOV operates as a rotating point force in acoustic media.

(ii) The effective dynamic size of the DOV is much smaller than a typical borehole diameter.

(iii) Due to its small dynamic size, DOV action in a borehole is effectively independent of the borehole wall geometry and elastic property heterogeneity.

(iv) In borehole operations DOV-generated acoustic waves appear as if diffracted from a slit of DOV axial cross-section.

(v) DOV-generated borehole acoustic waves convert at the borehole wall to *P* and *S* waves with frequency content 50–325 Hz and effective crosswell range up to 800 m.

(vi) DOV-generated seismic radiation peaks at low angles to the borehole axis normal.

(vii) In heterogeneous rock converted *S* waves are polarized both in-line and cross-line to the borehole axis.

(viii) Axially propagating tube waves are of order 10^{-3}–10^{-4} of the DOV wavelet amplitude.

(ix) Axially propagating body waves are of order 10^{-5}–10^{-6} of the DOV wavelet amplitude, indicating virtually no DOV shear coupling to borehole formations.

These features indicate that linear physical processes for DOV sourcing within a wellbore offers a high degree of wavelet stability for crosswell seismic time-lapse seismic monitoring of hydrocarbon production and related active seismic reservoir structure mapping. Stable converted *P*- and *S*-wave production focused at low angles to the plane of rotation and with without tube wave interference with crosswell range of order 1 km enable multiazimuth time-lapse crosswell surveys over borehole arrays to achieve essentially volumetric reservoir coverage.

ACKNOWLEDGMENTS

The DOV was re-engineered from the original Conoco orbital vibrator, a borehole source with suitably low levels of tube wave noise for effective borehole seismic imaging. Discussions with Jack Cole, Dale Cox, Don Howlett, John Queen, Stuart Crampin and Enru Li addressed initial work done with Conoco orbital vibrator. Acquisition of DOV test data in a New Mexico carbonate reservoir was possible through the cooperation of Tom Davis, Colorado School of Mines. The SMSITES Project run by Stuart Crampin (Crampin *et al.* 2003) supported DOV trials in open water and in tectonically active Iceland to provide basic data on DOV mechanics and wavelet stability. Rod Humphreys, Peter Jackson, John Gregson, Sebastien Chastin and Simon Wood contributed to SMSITES field work in the UK and Iceland. DOV crosswell seismic data at 650–800 m offsets in oilfield sediments were acquired in China during a project organized by William Ayres and executed by James Phillips, Nick Arend and Tony West with members of the Liaohe Geophysical Exploration Company. Tom Daley supplied helpful commentary on the original and revised manuscript; an anonymous reviewer influenced model presentation by noting an algebraic sign error in the original Appendix A; and a journal editor spurred more quantitative comparisons between models and data. We are grateful for the care and cooperation of all above.

REFERENCES

Aki, K. & Richards, P.G., 1980. *Quantitative Seismology*, W. H. Freeman, San Francisco.

Ayres, W., Leary, P.C. & Yang, W.J., 2003. Evidence for reservoir continuity in 650 m-offset crosswell seismic wave-guide signal, Expanded Abstract, EAGE 65th Conference & Exhibition, 2–5 June, Stavanger, Norway.

Claerbout, J.F., 1976. *Fundamentals of Geophysical Data Processing*, McGraw-Hill, New York.

Cole, J.H., 1997. The orbital vibrator, a new tool for characterizing interwell reservoir space, *The Leading Edge,* **16,** 281–283.

Crampin, S., Chastin, S. & Gao, Y., 2003. Shear-wave splitting in a critical crust: III. Preliminary report of multivariable measurements in active tectonics, *J. Appl. Geophys.,* **54,** 265–277.

Daley, T.M. & Cox, D., 2001. Orbital vibrator seismic source for simulataneous *P*- and *S*-wave crosswell acquisition, *Geophysic,* **66,** 1471–1480.

Daley, T.M., Gritto, R., Majer, E.J. & West, P., 2003. Tube-wave suppression in single-well seismic acquisition, *Geophysics,* **68,** 863–869.

Davis, T.L., Terrell, M.J., Benson, R.D., Cardona, R., Kendall, R.R. & Winarsky, R., 2003. Multicomponent seismic characterisation and monitoring of the CO_2 flood at Weyburn Field, Saskatchenwan, *The Leading Edge,* **22,** 696–697.

de Waal, H. & Calvert, R., 2003. Overview of global 4-D seismic implementation strategy, *Petroleum Geoscience,* **9,** 1–6.

Francis, A. & Pennington, W., 2001. Development and Production (Special Section), *The Leading Edge,* **20,** 269–328.

Jackson, D.D., 1962. *Classical Electrodynamics*, J Wiley & Sons, New York.

Leary, P.C., 2002a. Fractures and physical heterogeneity in crustal rock, in *Heterogeneity in the Crust and Upper Mantle*, pp. 155–186, eds Goff, J.A. & Holliger, K., Kluwer Academic/Plenum Publishers, New York/London.

Leary, P.C., 2002b. Numerical simulation of first-order backscattered *P*- and *S*-waves for time-lapse seismic imaging in heterogeneous reservoirs, *Geophys. J. Int.,* **148,** 402–425.

Leary, P.C. & Al-Kindy, F., 2002. Power-law scaling of spatially correlated porosity and log(permeability) sequences from north-central North Sea Brae oilfield well core, *Geophys. J. Int.,* **148,** 426–442.

Leary, P.C. & Walter, L.A., 2005. Physical model for the downhole orbital vibrator (DOV) – II. Rotary correlation wavelets and time-lapse seismics, *Geophys. J. Int.,* doi: 10.1111/j.1365-246X.2005.02771.x.

Li, G., 2003. 4-D seismic monitoring of CO_2 flood in a thin fractured carbonate reservoir, *The Leading Edge,* **22,** 690–695.

Liu, E., Crampin, S. & Queen, J.H., 1991. Fracture detection using reverse vertical seismic profiles and cross-hole surveys at the Conoco Borehole Test Facility, Oklahoma, *Geophys. J. Int.,* **107,** 449–463.

Liu, E., Crampin, S., Queen, J.H. & Rizer, W.D., 1993. Velocity and attenuation anisotropy caused by microcracks and macrofractures in azimuthal reverse VSPs, *Canadian J. Expl. Geophys.,* **29,** 177–188.

McInally, A.T., Redondo-Lopez, T., Garnham, J., Kunka, J., Brooks, A.D., Stenstrup Hansen, L., Barcaly, F. & Davies, D., 2003, Optimizing 4-D fluid imaging, *Petroleum Geoscience,* **9,** 91–102.

Oil & Gas Industry Task Force, 2001. Bringing research and technology to optimise reservoir performance, *First Break,* **19,** 351–365.

Parker, J., Bertelli, L. & Dromgoole, P., 2003, 4-D seismic technology special issue, *Petroleum Geoscience,* **9,** 1.

Press, W.H., Teukolsky, S.A., Vetterling, W.T. & Falnnery, B.P., 1992. *Numerical Recipes in Fortran*, 2nd edn, Cambridge University Press, p. 963.

Waters, K.H., 1981. *Reflection Seismology*, J Wiley & Sons, New York, p. 453.

APPENDIX A: THE POINT-FORCE MODEL ACOUSTIC WAVEFIELD

The displacement solution to the acoustic wave equation for a point force oscillating at frequency ω can be used to relate DOV acoustic wave pressures measured by a hydrophone in open water to the source motion measured by the monitor geophone. Let vector displacement motion $u_i(\boldsymbol{r}, t)$ be referred to a coordinate system in which the *instantaneous* DOV point force is aligned along the x-axis and the DOV axis lies along the z-axis. The polar angle θ relative to the x-axis determines the direction cosines $\gamma_i = [\cos\theta\,, 0, \sin\theta] = [x/r, 0, z/r]$ of radial motion with $\gamma_1 = \cos\theta = x/r$ focusing the radiation at small polar angles relative to plane of the rotating point force.

Following Section 4.2 of Aki & Richards (1980), the compressional wave displacement potential $\varphi(\boldsymbol{r}, t)$ excited by body-force $F_0(t)$ applied along the instantaneous x-axis is

$$\varphi(\boldsymbol{r}, t) = -1/(4\pi\rho)\partial_x(1/r)\int_0^{r/\alpha} d\tau\,\tau F_0(t-\tau). \tag{A1}$$

The resulting acoustic medium vector displacement $u_i(\boldsymbol{r}, t) = \partial_i\varphi(\boldsymbol{r}, t)$ is the sum of a far-field radiation term scaling as $1/r$ and a near-field term scaling as $1/r^3$,

$$\begin{aligned}
u_i(\boldsymbol{r}, t) &= -1/(4\pi\rho)\left\{\partial_i\partial_x(1/r)\int_0^{r/\alpha} d\tau\tau F_0(t-\tau) + \partial_1(1/r)\partial_i\int_0^{r/\alpha} d\tau\tau F_0(t-\tau)\right\}\\
&= -1/(4\pi\rho)\left\{\gamma_i\gamma_x/r^3\int_0^{r/\alpha} d\tau\tau F_0(t-\tau) + \gamma_i\gamma_1/r^2 1/\alpha^2\partial_r\int_0^{r} drr F_0(t-\tau)\right\}\\
&= -1/(4\pi\rho)\left\{\gamma_i\gamma_x/r^3\int_0^{r/\alpha} d\tau\tau F_0(t-\tau) + \gamma_i\gamma_1/r^2 1/\alpha^2[r F_0(t-r/\alpha)]_0^r\right\}\\
&= -1/(4\pi\rho)\gamma_i\gamma_x/r^3\int_0^{r/\alpha} d\tau\tau F_0(t-\tau) - 1/(4\pi\rho\alpha^2)\gamma_i\gamma_1/r\, F_0(t-r/\alpha)
\end{aligned} \tag{A2}$$

At any instant of time, acoustic wavefield (A2) is due to the acceleration of the DOV of mass m and displacement amplitude u_0 rotating at instantaneous angular frequency ω,

$$F_0(t-r/\alpha) = mu_0\omega^2\exp[i\omega(t-r/\alpha)]. \tag{A3}$$

The near-field term of (A2) for source function (A3) is

$$\begin{aligned}\int_0^{r/\alpha} d\tau\,\tau F_0(t-\tau) &= mu_0\omega^2\exp(i\omega t)\int_0^{r/\alpha} d\tau\,\tau\exp(-i\omega\tau)\\ &= mu_0\exp(i\omega t)\int_0^{kr} dkr\,kr\exp(-ikr)\\ &= mu_0\exp(i\omega t)i\left[\int_0^{kr} d[kr\exp(-ikr)] - \int_0^{kr} dkr\exp(-ikr)\right]\\ &= mu_0\exp(i\omega t)i\left[kr\,exp(-ikr)\big|_0^{kr} + i\exp(-ikr)\big|_0^{kr}\right]\\ &= mu_0\exp(i\omega t)[(1+ikr)\exp(-ikr)-1]. \end{aligned} \tag{A4}$$

From (A2)–(A4) with $k^2=\omega^2/\alpha^2$, the vector acoustic velocity field is

$$u_i(\boldsymbol{r},t) = -\gamma_i\gamma_x mu_0\exp(i\omega t)/(4\pi\rho)\{[(1+ikr)\exp(-ikr)-1]/r^3 - k^2/r\exp(-ikr)\}. \tag{A5}$$

Factoring the far-field term from (A5) and expressing the resulting effective dimension R_1 in terms of DOV density ρ_{dov} and volume $\pi a^2\ell$, $R_1 = k^2m/(4\pi\rho) = k^2\rho_{\mathrm{dov}}\pi a^2\ell/(4\pi\rho) = \pi^2\rho_{\mathrm{dov}}/\rho a^2\ell/\lambda^2 \approx 1$ mm, gives the far- and near-field velocity fields as

$$\begin{aligned} u_i(\boldsymbol{r},,t) &= u_0\gamma_i\gamma_x R_1/r[1-[(1+ikr)-\exp(ikr)](kr)^{-2}]\exp[i(\omega t-kr)]\\ &\approx 1/2u_0\gamma_i\gamma_x R_1/r\exp[i(\omega t-kr)],\quad (kr)^3 \ll 1. \end{aligned} \tag{A6}$$

In an unbounded acoustic medium, pressure $P(r)$ is related to the acoustic particle velocity by

$$\partial_t P(\boldsymbol{r},t) = -\rho\alpha^2\partial_i v_i(\boldsymbol{r},t) = -\rho\alpha^2\partial_t[\partial_x u_x(\boldsymbol{r},t)+\partial_z u_z(\boldsymbol{r},\,t)]. \tag{A7}$$

For radii closer to the DOV than the acoustic wavelength, $(kr)^3 \ll 1$, (A6) substituted into (A7) gives the model pressure field as a function of position $[x, 0, z]$,

$$\begin{aligned} P(\boldsymbol{r},\omega) &\approx -u_0\rho\alpha^2 R_1\left\{\partial_x[x^2\exp(-ikr)/r^3]+\partial_z[xz\exp(-ikr)/r^3]\right\}\\ &\approx i\gamma_x\rho u_0\omega^2 R_1\exp(-ikr)/(kr), \end{aligned} \tag{A8}$$

as essentially the pressure field of a monopole source for radial offsets greater than the source dimension $R_1 \approx 1$ mm.

Eqs (A1)–(A8) constrain DOV acoustic wavefield complexities at offsets greater than a few mm. It can, nonetheless, be hypothesized that within a borehole DOV dynamics exceeds the model (A1)–(A8) to create a dipole acoustic field of positive and negative pressures on opposite sides of the DOV. A borehole DOV dipole field can, it has been argued, cause shear distortion of the borehole that generates primary shear waves in the surrounding rock. Such a hypothetical dipole field is proportional to the difference of two monopole pressures located at opposing DOV radii,

$$P^{\mathrm{dipole}}(\boldsymbol{r},\omega) \propto i\gamma_x\rho u_0\omega^2 R_1 k^{-1}[\exp(-ikr_+)/r_+ - \exp(-ikr_-)/r_-], \tag{A9}$$

where $r_- = |\boldsymbol{r}+\boldsymbol{a}|$ is the distance from a monopole at $x=-a$ and $r_+ = |\boldsymbol{r}-\boldsymbol{a}|$ is the distance from a monopole at $x=+a$. The distances observed in open water are large compared with the DOV radius a, $r \gg a$, whence $r_- = |\boldsymbol{r}+\boldsymbol{a}| \approx r+\gamma a$ and $r_- = |\boldsymbol{r}-\boldsymbol{a}| \approx r-\gamma a$ where $\gamma = x/r$ is the instantaneous direction cosine, and (A9) reduces to

$$P^{\mathrm{dipole}}(r,\omega) \propto -i\gamma_x\rho u_0\omega^2 R_1\exp(-ikr)2a/r(1-i/kr). \tag{A10}$$

At distances $r \gg a$ and $\lambda \gg r$, the dipole kinematic field strength is less than the monopole kinematic strength, $2a/r \ll 1$. Dipole terms (A9)–(A10) thus provide no argument for the effect of a DOV dipole-source term at distances beyond the immediate vicinity of the DOV, $r \approx a$.

Fig. A1 compares the monopole and dipole fields near the DOV. The dipole terms are significant only for $[x \approx a,\ z \approx 0]$, where the point-force description of the DOV breaks down. However, it is seen in Section 4.1 that the symmetry of the 2-D laminar flow solution to the Navier-Stokes equation for a long cylinder disallows dipole conditions in the fluid. The point-force model thus provides no basis for significant dipole DOV action at operating frequencies. In absence of compelling observational evidence for DOV dipole terms (Section 4.2), a monopole source term with small effective dynamic scale $R_1 \approx 1$ mm appears to provide an adequate model for DOV source action in an acoustic medium.

APPENDIX B: KIRCHHOFF DIFFRACTION

The Kirchhoff approximation to diffraction of incident scalar wavefield $\psi_I(\boldsymbol{x}')$ at surface S is (Jackson 1962, pp. 292–294), (see Fig. B1)

$$\psi(x) \approx -\exp(ikr)/4\pi r\int_S \exp(-i\boldsymbol{k}\cdot\boldsymbol{x}')[\boldsymbol{n}\cdot\boldsymbol{\nabla}'\psi_I(\boldsymbol{x}') + i\boldsymbol{n}\cdot\boldsymbol{k}\psi_I(\boldsymbol{x}')]\,ds'.$$

The DOV acoustic radiation is the incident wavefield $\psi_I(\boldsymbol{x}')$ at diffraction source area S at position $x'=0$ with aperture $-d/2 \le y' \le d/2$, $\ell/2 \le z' \le \ell/2$, and DOV far-field radiation as diffracted wavefield $\psi(\mathbf{x})$. For $\boldsymbol{k} = k[\cos\theta, \sin\theta\cos\varphi, \sin\theta\sin\varphi]$, $\boldsymbol{n} = [1, 0, 0]$, $\boldsymbol{x}' = [0,$

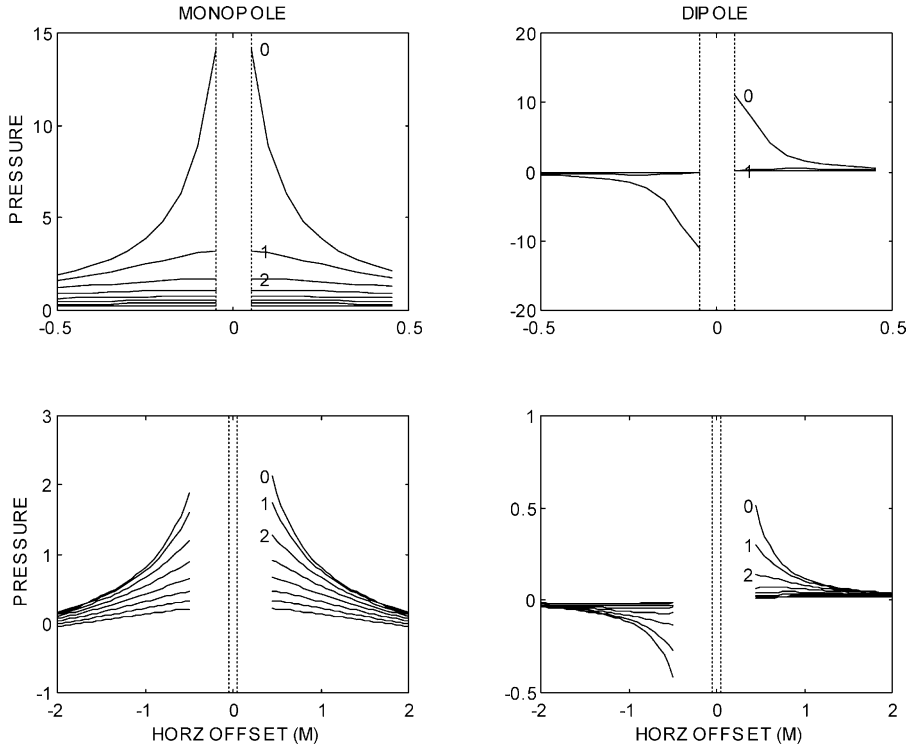

Figure A1. Symmetric and antisymmetric pressure fields for a monopole (left) and dipole (right) acoustic source. Families of solid lines denote pressure amplitude fall-off with radial offset as function of axial offset from the DOV centre; indices 0, 1, 2, denote sequence of axial offsets in 25 cm steps from initial 5 cm offset. Dashed lines denote DOV geometry with in the acoustic medium. Upper plots show near-DOV pressure curves; lower plots show pressure curves further from DOV. Antisymmetric acoustic pressure fields from DOV action in a borehole have been assumed to create shear tensions in the surrounding elastic medium. These figures, however, show no significant antisymmetric pressure fields along the DOV axis, consistent with failure to detect primary *S*-wave excitation by DOV action in a borehole.

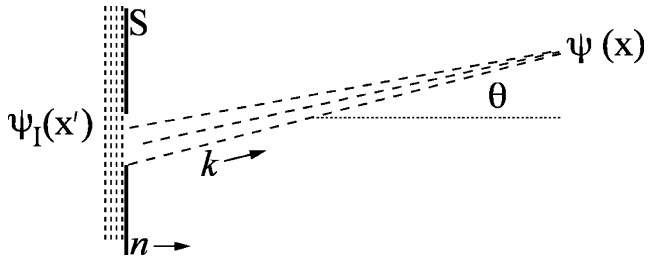

Figure B1. The process of Kirchhof wavefield diffraction at a slit defining plane surface *S*. For the DOV surface *S* is defined by the DOV length and borehole width.

$y', z']$,

$$\psi_I(\boldsymbol{x}') = \exp(i\boldsymbol{k}\cdot\boldsymbol{x}') = \exp[ik(x'\cos\theta + \sin\theta(y'\cos\varphi + z'\sin\varphi))$$
$$\boldsymbol{n}\cdot\boldsymbol{\nabla}'\psi_I(\boldsymbol{x}') = \partial_x \exp[ik(x\cos\theta + \sin\theta(y\cos\varphi + z\sin\varphi))|_{x=x'}$$
$$= ik\cos\theta\exp[ik\sin\theta(y'\cos\varphi + z'\sin\varphi))$$
$$i\boldsymbol{n}\cdot\boldsymbol{k}\psi_I(\boldsymbol{x}') = ik\cos\theta\exp[ik\sin\theta(y'\cos\varphi + z'\sin\varphi))$$

and the far-field radiation is

$$|\psi(x)| \approx |-2ik\cos\theta\exp(ikr)/4\pi r\int_S \exp(-i\boldsymbol{k}\cdot\boldsymbol{x}')[\exp(i\boldsymbol{k}\cdot\boldsymbol{x}')]\,dy'\,dz'|$$
$$\approx k\cos\theta|\exp(ikr)|/2\pi r[d/2-(-d/2)][\ell/2-(-\ell/2)]$$
$$\approx 2\pi/\lambda\cos\theta/2\pi r\ell d$$
$$\approx (\ell/r)(d/\lambda)\cos\theta.$$

APPENDIX C: ACOUSTIC STREAMLINE VELOCITY FIELD SURROUNDING DOV

Approximating DOV action as instantaneous steady flow, the velocity potential in the fluid is

$$\phi = \mathring{u} a^2 / r \cos\theta, \tag{C1}$$

where θ is the angle from the direction $\boldsymbol{x}$ of cylinder instantaneous motion through the fluid, and $r > a$ is the radial distance from the cylinder centre. In Cartesian coordinates, $r^{-1} \cos\theta = x/(x^2 + y^2)$ and the vector velocity field in the fluid is

$$\begin{aligned} \boldsymbol{v} = \nabla\phi &= \mathring{u} a^2 \left[\partial_x (x/(x^2+y^2))\boldsymbol{x} + \partial_y (x/(x^2+y^2))\boldsymbol{y}\right] \\ &= \mathring{u} a^2 / r^2 [(1 - 2\cos^2\theta)\boldsymbol{x} + 2\sin\theta\cos\theta\boldsymbol{y}] \\ &= \mathring{u} a^2 / r^2 [\cos 2\theta \boldsymbol{x} + \sin 2\theta \boldsymbol{y}] \end{aligned} \tag{C2}$$

The instantaneous fluid velocity potential function satisfies Laplace's equation for zero divergence of the velocity field: $\nabla \cdot \boldsymbol{v}(x, y) \propto \partial_x((\cos 2\theta)/r^2) + \partial_y((\sin 2\theta)/r^2) = \partial_x((x^2 - y^2)/r^4) + \partial_y(2xy)/r^4) = 2x/r^4 - 2(2x)(x^2 - y^2)/r^6 + 2x/r^4 - 2(2y)2xy/r^6 = 1/r^6\,[4x(x^2 + y^2) - 4x(x^2 - y^2) - 8xy^2] = 0$.

The fluid velocity normal to the DOV surface equals the velocity of the DOV in the normal direction. For DOV normal $\boldsymbol{n} = \cos\theta\boldsymbol{x} + \sin\theta\boldsymbol{y}$,

$$\begin{aligned} \boldsymbol{n} \cdot \boldsymbol{v}(r = a, \theta) &= u_0 (a/a)^2 [(\cos 2\theta)\cos\theta + (\sin 2\theta)\sin\theta] \\ &= u_0 \cos\theta [\cos^2\theta - \sin^2\theta + 2\sin^2\theta] \\ &= u_0 \cos\theta. \end{aligned}$$